



Cite this: *CrystEngComm*, 2021, 23, 1497

Luminescence sensing and photocatalytic activities of four Zn(II)/Co(II) coordination polymers based on a pyridinephenyl bifunctional ligand†

Yun-Shan Xue,^{‡a} Chen Zhang,^{‡a} Jun Qing Lv,^a Ning-Ning Chen,^a Jun Wang,^{id}^{*a} Xuan-Rong Chen^a and Liming Fan^{id}^{*b}

Based on a novel pyridinephenyl bifunctional ligand of 5-(6-carboxypyridin-2-yl)benzene-1,3-dicarboxylic acid (H₃L), four Zn(II)/Co(II) coordination polymers (CPs), {[Zn(BIMB)(HL)]·H₂O}_n (**1**), [Co(BIMB)(HL)(H₂O)]_n (**2**), {[Zn₂(BIBP)₂(HL)₂·2H₂O]_n (**3**), and {[Co₃(BIBP)₃(L)₂(H₂O)₂·5H₂O]_n (**4**), have been constructed with the introduction of two length-suitable bis(imidazole) linkers (BIMB = 4,4-bis(imidazol-1-yl)methyl)biphenyl; BIBP = 4,4-bis(imidazol-1-yl)diphenyl). Structural analysis shows that CP **1** exhibits a 2D wave 4-c {4⁴·6²} **sql** sheet, and CP **2** shows an interesting 2D + 2D → 2D interpenetrating structure with ABAB **sql** packing. CP **3** displays an unprecedented 3D (4,4)-c {4²·8³·10}-**tcj** net. CP **4** presents a 2D (3,4,4)-c {6²·7·8²·10} {6²·7³·8}₂{6³}₂ trilayer structure reported for the first time. Luminescence sensing exploration reflected two luminescent Zn(II) CPs possessing excellent performances in sensing Fe³⁺ cation, Cr₂O₇²⁻/CrO₄²⁻ anions, and NFT/NZF antibiotics in aqueous solution. Besides, the four obtained CPs also demonstrated outstanding potential as photocatalysts in the degradation of methylene blue (MB).

Received 15th December 2020,
Accepted 11th January 2021

DOI: 10.1039/d0ce01812k

rsc.li/crystengcomm

Introduction

As we all know, water pollution is closely related to industrial development since modern times, which seriously endangers the health of human beings and life. The harmful substances in sewage finally enter through the food chain and the natural water cycle.^{1,2} Thus, appropriate detection and rapid removal is essential and necessary. At present, the common traditional detection methods, such as gas chromatography (GC), high performance liquid chromatography (HPLC), mass spectrometry (MS), and electrochemical analysis (EA) seem to be in the ascendancy. However, the disadvantages of high cost, time-consuming, limited portability, and complex operation make it impossible for further application.³ The removal of pollutants can achieve through the effective adsorption of porous materials. Meanwhile, this normal operation often has the problems of hard controlling, smaller

scale, high operation costs, and secondary pollution.⁴ The design of novel materials for the rapid detection and removal of contaminants in water has become an important necessity.

Coordination polymers (CPs), as the representative of most popular organic-inorganic hybrid materials, have attracted considerable attention not only due to the unique features, such as adjustable channels, modifiable structures, multiple active sites, but also outstanding performances and potential applications in photo-catalysis,^{5,6} gas capture and storage,^{7,8} drug delivery,⁹ magnetism,^{10,11} and catalysis,^{12,13} especially in the field of sensing.^{14–21} According to materialistic dialectics, the diverse properties are the objective reflections of structures, indicating that more CPs with versatile structures and functionality could be constructed by the deliberate design and selection of organic linkers and inorganic units.^{22–25} Here, the novel pyridinephenyl bifunctional ligand of 5-(6-carboxypyridin-2-yl)benzene-1,3-dicarboxylic acid (H₃L) was selected to react with Zn(II)/Co(II) salts because the pyridinephenyl bifunctional ligands are inclined to form various frameworks with uncoordinated N or O active sites. Besides, the length-suitable bis(imidazole) linkers are selected to expand their dimensions.^{26–31} Of course, the advantages of the mixed ligand strategy are also under consideration.^{32–37}

Fortunately, here four Zn(II)/Co(II) CPs with distinct structures, ranging from wave 4-c {4⁴·6²} **sql** sheet (**1**), 2D +

^a School of Chemistry & Environmental Engineering, Yancheng Teachers University, Yancheng 224007, China. E-mail: wjyctu@hotmail.com

^b Department of Chemistry, College of Science, North University of China, Taiyuan 030051, China. E-mail: limingfan@nuc.edu.cn

† Electronic supplementary information (ESI) available: Additional figures, PXRD patterns, TG curves, and X-ray crystallographic data, CCDC 1991806–1991809 for **1–4**. CCDC 1991806–1991809. For ESI and crystallographic data in CIF or other electronic format see DOI: 10.1039/d0ce01812k

‡ The authors contributed equally to this work.

2D \rightarrow 2D interpenetrating structure with ABAB **sql** packing (2), 3D (4,4)-c $\{4^2 \cdot 8^3 \cdot 10\}$ -**tcj** net (3), to 2D (3,4,4)-c $\{6^2 \cdot 7 \cdot 8^2 \cdot 10\}$ $\{6^2 \cdot 7^3 \cdot 8\}_2\{6^3\}_2$ trilayer (4), were constructed from the pyridinephenyl bifunctional ligand of 5-(6-carboxypyridin-2-yl)benzene-1,3-dicarboxylic acid (H_3L) and two bis(imidazole) linkers (BIMB = 4,4-bis(imidazol-1-ylmethyl)biphenyl; BIBP = 4,4-bis(imidazol-1-yl)diphenyl) for the first time (Schemes 1, and S1†). Further luminescence sensing exploration displayed that the two luminescent Zn(II) CPs have excellent sensing performances and can be used as chemical sensors for selective detection of Fe^{3+} ion, $Cr_2O_7^{2-}/CrO_4^{2-}$ anions, and NFT/NZF antibiotics in aqueous solution. Besides, the four obtained CPs also demonstrated outstanding potential as photocatalysts in the degradation of methylene blue (MB).

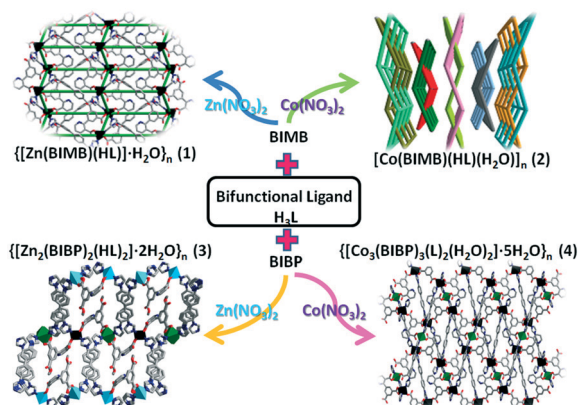
Experimental section

Materials and methods

5-(6-Carboxypyridin-2-yl)benzene-1,3-dicarboxylic acid, 4,4-bis(imidazol-1-yl)diphenyl, 4,4-bis(imidazol-1-ylmethyl)biphenyl, $Zn(NO_3)_2 \cdot 6H_2O$, $Co(NO_3)_2 \cdot 6H_2O$, and common solvents were commercially purchased and used without further purification. Other testing methods, including the collection and refinement of single-crystal X-ray diffraction data, are the same as reported.^{38,39} The crystallographic data as well as the selected bond distances/angles for 1–4 are listed in Tables S1 and S2† with the CCDC numbers being 1991806 for 1, 1991807 for 2, 1991808 for 3, and 1991809 for 4.

Synthetic routes

The titled CPs were synthesized as given in Scheme 1 by mixing the metal nitrate, H_3L , the bis(imidazole) linkers in the solvents and stirring at room temperature for a quarter of an hour. Then, the mixture was sealed in a 10 mL Teflon-lined stainless steel vessel and heated at 100 °C for 3 days to obtain the CPs. The detailed routes are given in the experimental section of the ESI.†



Scheme 1 The synthetic routes of the four titled complexes.

Results and discussion

Structural description of $\{[Zn(BIMB)(HL)] \cdot H_2O\}_n$ (1)

Crystallographic analysis indicates that CP 1 crystallizes in the monoclinic form with $P2_1/c$ (14) space group. The asymmetric unit of CP 1 consists of one crystallographically independent Zn^{II} ion, one partially deprotonated HL^{2-} ligand, one neutral BIMB linker, and one free water molecule. The central Zn^{II} ion lies in the $\{ZnN_2O_2\}$ tetrahedron geometry with the τ_4 being 0.84(7), surrounded by two carboxyl oxygen atoms (O1 and O5A) as well as two imidazolyl nitrogen atoms (N2 and N5B) (Fig. 1a).

The bifunctional H_3L ligand adopts $(\kappa^1-\kappa^0)-(\kappa^1-\kappa^0)-\mu_2$ mode (mode I, Scheme S2† with the dihedral angle being 30.06° between the phenyl ring and pyridine ring) in the formation of CP 1 by partial deprotonation, acting as the bridging linker to connect the Zn^{II} ions to make a 1D helix $[Zn(HL)]_n$ chain with a $Zn \cdots Zn$ distance of 7.815(1) Å (Fig. 1b). Meanwhile, the neutral BIMB linkers bridge the Zn^{II} cations to leave a 1D $[Zn(BIMB)]_n$ chain with a $Zn \cdots Zn$ distance of 15.679(1) Å (Fig. S1†). Sharing those Zn^{II} ions, a 2D wave layer of 1 was constructed and is given in Fig. 2. After simplifying by using the software of TOPOS, the 2D layer was simplified as a 4-c $\{4^4 \cdot 6^2\}$ **sql** net (Fig. S2†).⁴⁰ With the help of strong O–H \cdots O and C–H \cdots O hydrogen bonds (Table S3†), those 2D wavy sheets expanded into a 3D supramolecular structure, in which the lattice water molecules act as interesting relay nodes of hydrogen bonding effects, and also play an important role in maintaining structural stability (Fig. S3†).

Structural description of $[Co(BIMB)(HL)(H_2O)]_n$ (2)

When $Co(NO_3)_2 \cdot 6H_2O$ replaced $Zn(NO_3)_2 \cdot 6H_2O$ and was introduced into the reaction system, a different 2D sheet was constructed. CP 2 also crystallizes in the space group of monoclinic $P2_1/c$ (14), and its asymmetric unit contains one cobalt(II) cation, one partially deprotonated HL^{2-} ligand, one neutral BIMB linker, as well as one coordinated water molecule. The Co^{II} ion occupies the centre of a distorted $\{CoO_4N_2\}$ octahedron geometry, embraced by two imidazolyl nitrogen atoms (N1, and N4B), three carboxyl oxygen atoms

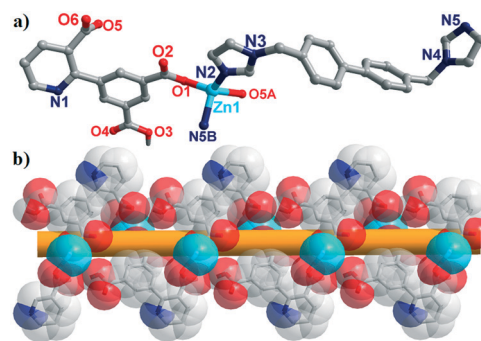


Fig. 1 (a) Coordination environment of the Zn^{II} cation in 1 (symmetry codes: A: $-x + 2, y + 1/2, -z + 1/2$; B: $x + 1, y, z$). (b) The 1D helix $[Zn(HL)]_n$ chain in 1.

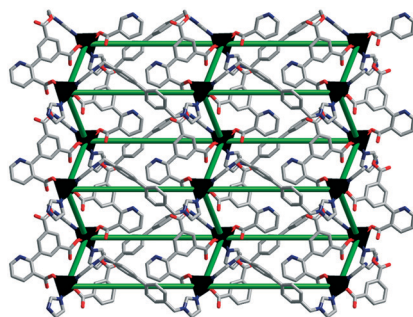


Fig. 2 The 2D sheet of **1** with the 4-c $\{4^4 \cdot 6^2\}$ sqf layer.

(O1, O6C, and O7C), and one coordinated water molecule (O5) (Fig. 3).

The partially deprotonated HL^{2-} ligand adopted $(\kappa^1-\kappa^0)-(\kappa^1-\kappa^1)-\mu_2$ mode (mode II, Scheme S2,† the dihedral angle being 38.13°) in **2** to link the Co^{II} cations to generate a 1D $[\text{Co}(\text{HL})]_n$ chain, in which the $\text{Co}\cdots\text{Co}$ distance is $10.620(1)$ Å (Fig. S4†). In the meantime, the neutral BIMB linkers fit those Co^{II} cations together to give a 1D $[\text{Co}(\text{BIMB})]_n$ chain with a $\text{Co}\cdots\text{Co}$ distance of $18.142(1)$ Å (Fig. S5†). Those two kinds of chains interweaved through sharing the central Co^{II} cations to give a 2D layer (Fig. 4a). It is remarkable that the two 2D layers interpenetrated each other, leaving 2D + 2D \rightarrow 2D interpenetrating sheets (Fig. S6†). From the perspective of topology, CP **2** is an interesting 2D + 2D \rightarrow 2D interpenetrating sqf sheet with ABAB packing, with Co^{II} cations regarded as 4-c nodes (Fig. 4b). Those interpenetrating layers further expanded into a 3D supramolecular structure (Fig. S7†) through hydrogen bonding interactions (Table S4†).

Structural description of $[\{\text{Zn}_2(\text{BIBP})_2(\text{HL})_2\} \cdot 2\text{H}_2\text{O}]_n$ (**3**)

Different from the flexible bis(imidazole) linker of BIMB, when **3** was designed, the rigid bis(imidazole) linker of BIBP was selected for the reaction system, and a distinct structure was obtained here. CP **3** crystallizes in the crystal system of orthorhombic with the space group of $Pnn2$ (34). As displayed in Fig. 5, there are two zinc(II) cations (including one Zn1 cation, a half of Zn2 cation, and a half of Zn3 cation), two

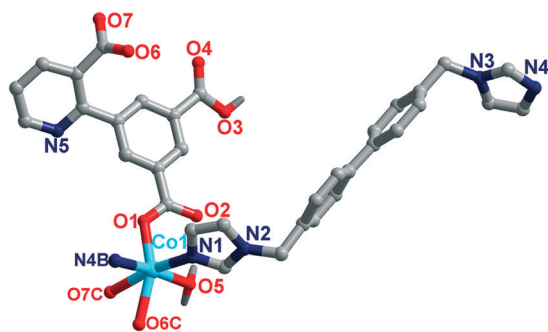


Fig. 3 Coordination environment of Co^{II} cation in **2** (symmetry codes: B: $1 + x, 3/2 - y, -1/2 + z$; C: $x, y, -1 + z$).

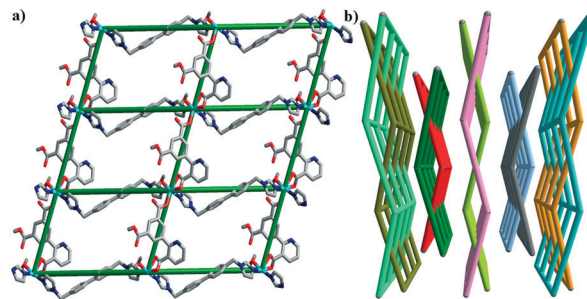


Fig. 4 (a) 2D sheet and (b) 2D + 2D \rightarrow 2D interpenetrating sheets of **2**.

different HL^{2-} ligands, two rigid neutral BIBP linkers, as well as two lattice water molecules in the asymmetric unit of CP **3**. Zn1 and Zn2 lie in a similar distorted $\{\text{ZnN}_2\text{O}_2\}$ tetrahedral geometry, both encircled by two carboxyl oxygen atoms (O1 and O6B for Zn1, O7 and O7D for Zn2) of two distinct HL^{2-} ligands and two imidazolyl nitrogen atoms (N3, N7 for Zn1, and N6, N6D for Zn2) from two different BIBP linkers, with the τ_4 being $0.92(5)$ for Zn1, and $0.90(1)$ for Zn2, respectively. While Zn3 is located in a C_2 -symmetric $\{\text{ZnN}_2\text{O}_4\}$ geometry, surrounded by four carboxyl oxygen atoms (O9A, O9B, O10A, and O10B) from two different HL^{2-} ligands, as well as two imidazolyl nitrogen atoms (N10, and N10C) from two BIBP linkers.

In the assembly of CP **3**, there are two kinds of HL^{2-} ligands adopting $(\kappa^1-\kappa^1)-(\kappa^1-\kappa^0)-\mu_2$ mode (mode III, Scheme S2,† the dihedral angle being 47.04°) and $(\kappa^1-\kappa^0)-(\kappa^1-\kappa^0)-\mu_2$ mode (mode I, Scheme S2,† the dihedral angle being 46.68°) to connect the Zn^{II} cations, giving two similar 1D $[\text{Zn}(\text{HL})]_n$ chains with the nearest $\text{Zn}\cdots\text{Zn}$ distances of $8.126(3)$ Å for $\text{Zn1}\cdots\text{Zn1B}$, and $7.685(9)$ Å for $\text{Zn3}\cdots\text{Zn3A}$, respectively (Fig. S8†). At the same time, the rigid BIBP linkers bridged the Zn^{II} cations to construct a 1D wave $[\text{Zn}(\text{BIBP})]_n$ chain with a $\text{Zn}\cdots\text{Zn}$ distance of $17.598(2)$ Å for $\text{Zn1}\cdots\text{Zn2}$, and $17.600(1)$ Å for $\text{Zn1}\cdots\text{Zn3}$, respectively (Fig. S9†). Sharing those central Zn^{II} cations, the 3D framework of CP **3** was obtained (Fig. 6a). From the point of view of topology, the Zn^{II} ions can be simplified as 4-connected nodes, while the HL^{2-} and BIBP ligands are considered as simple linkers. Thus, the above mentioned framework can be represented as a 3D 2-nodal (4,4)-net with stoichiometry (4-c)(4-c) (Fig. 6b and S10†). The point (Schlafli) symbol for the framework is

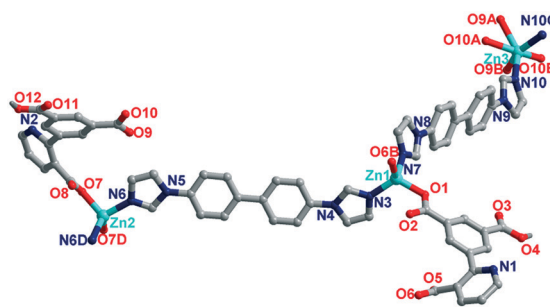


Fig. 5 The asymmetric unit of **3** (symmetry codes: A: $1/2 - x, 1/2 + y, -1/2 + z$; B: $-1/2 + x, 3/2 - y, -1/2 + z$; C: $-x, 2 - y, z$; D: $2 - x, 1 - y, z$).

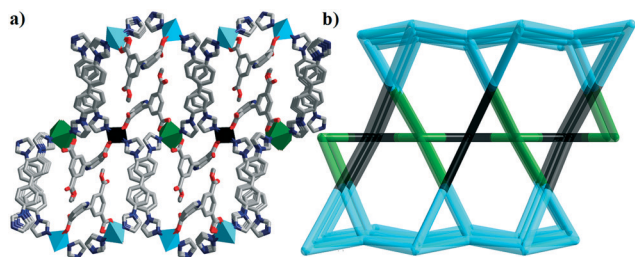


Fig. 6 (a) The 3D framework of **3**; (b) the simplified 3D (4,4)-c $\{4^2\cdot 8^3\cdot 10\}$ tctj net of **3**.

$\{4^2\cdot 8^3\cdot 10\}$, with the topological type being an unprecedented **tctj**, which are rarely reported in coordination chemistry.

Structural description of $[\text{Co}_3(\text{BIBP})_3(\text{L})_2(\text{H}_2\text{O})_2]\cdot 5\text{H}_2\text{O}]_n$ (**4**)

CP **4** crystallizes in the *Pccn* (56) space group of the orthorhombic crystal system, with its asymmetric unit containing one and a half of cobalt(II) cations, one L^{3-} ligand, one and a half of rigid neutral BIBP linkers, one coordinated water molecule, and two and a half of lattice water molecules. There are two kinds of Co^{II} cations, with the occupancies of 1 for Co1 and 0.5 for Co2, respectively. As displayed in Fig. 7, every Co1 is surrounded by two imidazolyl nitrogen atoms (N2 and N7B) from two different BIBP linkers, three oxygen atoms from two L^{3-} ligands (O1, O3C, and O4C), and one coordinated water molecule (O7), leaving a distorted $\{\text{CoN}_2\text{O}_4\}$ octahedron geometry. While Co2 is C_2 -symmetric and tetra-coordinated by two carboxyl oxygen atoms (O6, and O6D) from two different L^{3-} ligands and two imidazolyl nitrogen atoms (N4, and N4D), leaving a distorted $\{\text{CoO}_2\text{O}_2\}$ tetrahedron geometry with the τ_4 being 0.73(9).

With three carboxyl groups, all deprotonated, each L^{3-} ligand acts as a tripodal linker to join three Co^{II} cations to form a 2D $[\text{Co}_3(\text{L})_2]_n$ sheet (Fig. S11[†]), in which the L^{3-} ligand adopts a $(\kappa^1\text{-}\kappa^0)\text{-}(\kappa^1\text{-}\kappa^1)\text{-}(\kappa^1\text{-}\kappa^0)\text{-}\mu_3$ coordination mode (mode IV, Scheme S2[†], the dihedral angle is 33.89°). Meanwhile, the rigid neutral BIBP linkers bridged the Co^{II} cations to acquire a 1D $[\text{Co}(\text{BIBP})]_n$ chain (Fig. S12[†]), with the BIBP separated $\text{Co}\cdots\text{Co}$ distance of 16.630(4) Å for $\text{Co1}\cdots\text{Co1A}$ (symmetry code: A: $0.5 - x, 0.5 - y, z$) and 17.440(3) Å for $\text{Co2}\cdots\text{Co1E}$ (symmetry code: E: $1 + x, y, z$), respectively. Sharing the central Co^{II} ions, a trilayer sheet of **4** was constructed

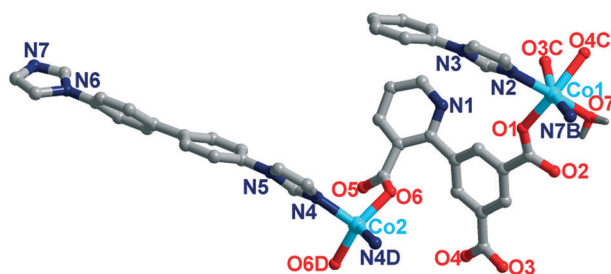


Fig. 7 Coordination environments of Co^{II} ions in **4** (symmetry codes: B: $-1 + x, y, z$; C: $-x, -1/2 + y, 1/2 - z$; D: $1/2 - x, 3/2 - y, z$).

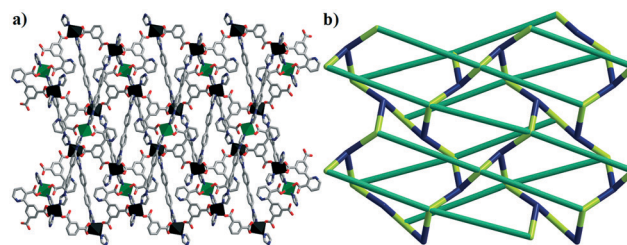


Fig. 8 (a) The 2D trilayer structure of **4** with the dark tetrahedron for Co1, green tetrahedron for Co2; (b) the (3,4,4)-c $\{6^2\cdot 7\cdot 8^2\cdot 10\}$ $\{6^2\cdot 7^3\cdot 8\}_2\{6^3\}_2$ topology of **4**.

(Fig. 8a). Topologically, the above mentioned trilayer was considered as a 3-nodal 3,4,4-c net when the Co^{II} cations were simplified to 4-connected nodes, and the L^{3-} ligands were simplified as 3-connected nodes, respectively (Fig. 8b). The point (Schläfli) symbol of the calculated topology is $\{6^2\cdot 7\cdot 8^2\cdot 10\}\{6^2\cdot 7^3\cdot 8\}_2\{6^3\}_2$. The main forces to push the trilayer sheets into a 3D supramolecular structure (Fig. S13[†]) are the $\text{O}\cdots\text{H}\cdots\text{O}$ hydrogen bonds (Table S5[†]) and the $\pi\cdots\pi$ packing interactions between the phenyl rings and the imidazolyl rings (Fig. S14[†]).

X-ray powder diffraction analyses and thermal analyses

In order to provide the basis for subsequent testing, the phase purity of **1–4** was measured using the powder X-ray diffraction analyses at room temperature. As shown in Fig. S15[†], experimental PXRD patterns matched well with the simulated ones, which were obtained from the single-crystal data using the Mercury software, disclosing that the obtained CPs hold good phase purity.

To further study the thermal stability of the titled CPs, the powder crystals of **1–4** were tested under N_2 atmosphere with the temperature ranging from atmospheric temperature to 800°C . TG curves are given in Fig. S16[†] for **1**, and the free water molecules are completely lost at 130°C (obsd: 2.48%; calcd: 2.64%). The framework is stable in the temperature range up to 340°C , with the main residue of 11.93% of ZnO (calcd: 11.92%). For **2**, the first weight loss of 2.29% is detected before 118°C , mainly due to the loss of the coordinated water (calcd: 2.66%), and then the skeleton framework starts to decompose at about 300°C . The remaining weight of 12.01% is of CoO, which is in agreement with the calculated value of 11.08%. For **3**, the first weight loss of 2.31% (calcd: 2.75%) from room temperature to 115°C corresponds to the loss of the free water molecules. The following second part of mass loss from 175°C to 660°C can be assigned to the decomposition of the organic linkers. The remaining residue may be ascribed to ZnO, showing a final mass of 12.95% (calcd: 12.43%). For **4**, the 6.92% weight loss (calculated 7.29%) in the temperature range of $80\text{--}160^\circ\text{C}$ corresponds to the release of the lattice and coordinated water molecules, and the remaining solid framework remains stable till a temperature of up to 340°C . With the increasing

temperature, the remaining residue tends to form CoO (obsd: 12.01% and calcd: 12.99%).

Luminescence properties

The solid state photoluminescence properties of two Zn(II) CPs, as well as the free H₃L ligand, are investigated at atmospheric temperature (Fig. S17†). The main emission peak of the H₃L ligand is observed at 370 nm ($\lambda_{\text{ex}} = 270$ nm), attributed to the $n/\pi \rightarrow \pi^*$ electron transitions.⁴¹ CP 1 and 3 exhibit emission bands with maxima at 375 nm and 380 nm under the same excitation wavelength. Taking into consideration the d^{10} configuration of Zn(II) cations, those emissions are neither metal-to-ligand charge transfer (MLCT) nor ligand-to-metal transfer (LMCT).⁴² The slightly red-shifted emission bands of 1 and 3 can mainly be assigned to the coordination effects.⁴³

Selective detection of Fe³⁺ cation

Considering the excellent solid state fluorescence properties of the titled two Zn(II) CPs, the potential sensing and detection abilities of 1 and 3 for metal ions in aqueous solution were explored. Thus, the suspension fluorescence of 1 and 3 were measured by dispersing in water. As seen from Fig. S17b,† compounds 1 and 3 exhibit strong emissions centred at 369 and 375 nm, respectively. Compared to solid fluorescence, the suspension fluorescence of 1 and 3 showed a blue shift of 6 and 5 nm. This phenomenon might be attributed to solvent effects, which is caused by the formation of intermolecular interactions between the water molecules and the frameworks.^{44–46} The selective sensing abilities of 1 and 3 for Fe³⁺ ions were explored by using 5 mg ground powder samples scattered into a 3 mL 10 mM M(NO₃)_n aqueous solution (M = Na⁺, Ag⁺, Li⁺, Co²⁺, Zn²⁺, Ni²⁺, Mg²⁺, Pb²⁺, Cd²⁺, Ca²⁺, Cu²⁺, Al³⁺, Cr³⁺, and Fe³⁺), and then the mixture was treated for 30 min by an ultrasound method to ensure dispersion. As viewed from Fig. 9 and S18,† the luminescence intensities of 1 and 3 are almost completely quenched in the above mentioned Fe³⁺ aqueous solution. Then, the gradient titration luminescence measurements were carried out to further check the sensitivity of 1 and 3 toward Fe³⁺.

As displayed in Fig. 10a and b, the fluorescence intensities of 1 and 3 dropped dramatically with increasing Fe³⁺ concentration. The quenching efficiency was quantitatively evaluated by using the Stern–Volmer equation: $I_0/I = 1 +$

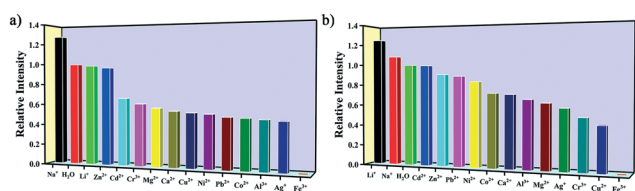


Fig. 9 The relative fluorescence intensity of 1 (a) and 3 (b) toward metal cations in aqueous solution.

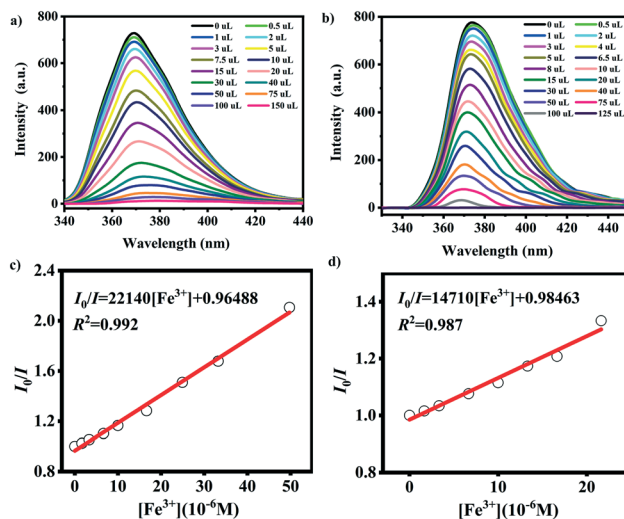


Fig. 10 Variation of luminescence intensities of 1 (a) and 3 (b) titrated with Fe(NO₃)₃ and the Stern–Volmer plots of Fe³⁺ in 1 (c) and 3 (d).

$K_{\text{SV}}[Q]$, where I_0 and I correspond to luminescence intensities without and with the addition of Fe³⁺ cation, and $[Q]$ is the concentration of the Fe³⁺ cation in aqueous solution. As observed from Fig. 10c and d, the I_0/I and the concentration of Fe³⁺ cations show good linear relationships ($R^2 = 0.992$ for 1 and $R^2 = 0.987$ for 3) at low concentration, with related quenching constants (K_{SV}) of $2.21 \times 10^4 \text{ M}^{-1}$ for 1, and $1.47 \times 10^4 \text{ M}^{-1}$ for 3, respectively. The related detection limits (LOD) for Fe³⁺ cations are obtained according to the formula of $3\delta/k$ (where δ is the standard deviation for five cycle luminescence tests using a blank solution, k is quenching constant), with the LOD being $2.29 \times 10^{-5} \text{ M}$ for 1 and $3.32 \times 10^{-5} \text{ M}$ for 3 (Tables S6 and S7†). Compared with recently reported CP based luminescent sensors, 1 and 3 show lower LODs in the detection of Fe³⁺ cations (Table S8†).^{47–51} Anti-interference experiments also were extended by injecting the Fe³⁺ cations into the suspension of 1 and 3 containing five random groups of mixed metal cations (Ag⁺/Na⁺/Co²⁺, Li⁺/Ni²⁺/Zn²⁺, Mg²⁺/Pb²⁺/Cd²⁺, Cr³⁺/Ca²⁺, Al³⁺/Cu²⁺, the concentration is 0.01 M) aqueous solutions, and the results are given in Fig. S19,† indicating that both 1 and 3 show good anti-interference in the detection of Fe³⁺ cations.

Selective detection of Cr₂O₇²⁻/CrO₄²⁻ anions

The same test process as that for metal cations was tested here to investigate the sensing properties of two Zn(II) CPs towards anions by using 0.01 M Na_nX aqueous solutions (X = Br⁻, SCN⁻, NO₃⁻, H₂PO₄⁻, HCO₃⁻, SO₄²⁻, CO₃²⁻, C₂O₄²⁻, HPO₄²⁻, PO₄³⁻, CrO₄²⁻, and Cr₂O₇²⁻). Interestingly, the luminescence of 1 and 3 reduce vastly in the case of CrO₄²⁻ and Cr₂O₇²⁻, leading to fluorescence quenching without obvious effects on the emission for other anions (Fig. 11 and S20†).

The titration experiments with different chromate anion concentrations are further conducted to learn the

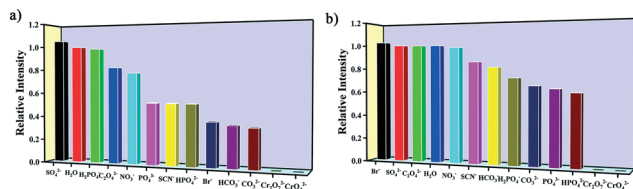


Fig. 11 Fluorescence relative intensity of **1** (a) and **3** (b) toward different anions in H₂O solution.

luminescence responses of the two titled Zn(II) CPs to chromate anions. As can be seen in Fig. 12a and b and Fig. 13a and b, the significant fluorescence intensity variations of **1** and **3** are observed with the gradual increase of chromate anion concentrations. On the basis of Stern–Volmer equation, the linear correlations appeared (Fig. 12c and d and Fig. 13c and d), and the calculated values of the quenching constant K_{SV} are $2.08 \times 10^4 \text{ M}^{-1}$ ($R^2 = 0.993$) for $\text{Cr}_2\text{O}_7^{2-}$ and $1.70 \times 10^4 \text{ M}^{-1}$ ($R^2 = 0.986$) for CrO_4^{2-} by **1**. The K_{SV} values are $1.34 \times 10^4 \text{ M}^{-1}$ ($R^2 = 0.996$) for $\text{Cr}_2\text{O}_7^{2-}$ and $1.20 \times 10^4 \text{ M}^{-1}$ ($R^2 = 0.991$) for CrO_4^{2-} by **3**. The detection limits for $\text{Cr}_2\text{O}_7^{2-}/\text{CrO}_4^{2-}$ are $2.51 \times 10^{-5} \text{ M}/2.67 \times 10^{-5} \text{ M}$ for **1** and $3.34 \times 10^{-5} \text{ M}/4.16 \times 10^{-5} \text{ M}$ for **3**, respectively (Tables S6 and S7†). The LODs of **1** and **3** are comparable to those of previously reported CPs for the detection of $\text{Cr}_2\text{O}_7^{2-}/\text{CrO}_4^{2-}$ ions (Table S8†).^{52–62} Like the related investigation of anti-interference effects of metal cations to Fe^{3+} above, here the anti-interference effects of other anions to Cr(VI) anions were also evaluated, with the results given in Fig. S21,† indicating that the quenching selectivity of **1** and **3** for $\text{Cr}_2\text{O}_7^{2-}/\text{CrO}_4^{2-}$ is not disturbed by the addition of other anions. **1** and **3** show good selectivity toward $\text{Cr}_2\text{O}_7^{2-}/\text{CrO}_4^{2-}$ in the presence of other anions.

Sensing of NZF/NFT antibiotics

Inspired by the good photo-luminescence behaviour of **1** and **3**, the performances of **1** and **3** for the fluorescence detection

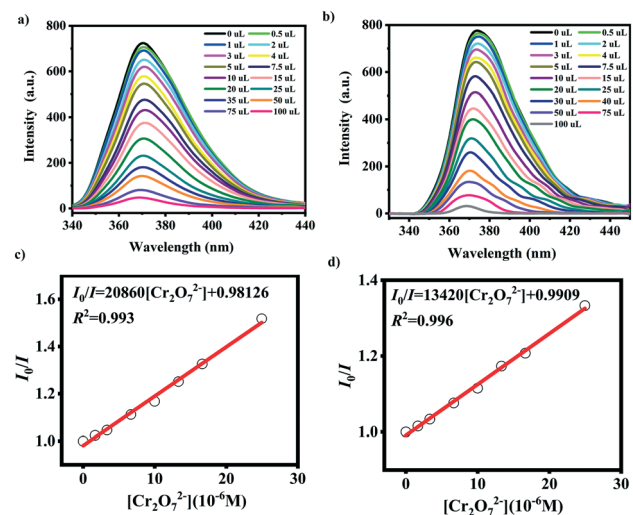


Fig. 12 Variation of luminescence intensities of **1** (a) and **3** (b) titrated with $\text{Na}_2\text{Cr}_2\text{O}_7$ and the Stern–Volmer plots of $\text{Cr}_2\text{O}_7^{2-}$ in **1** (c) and **3** (d).

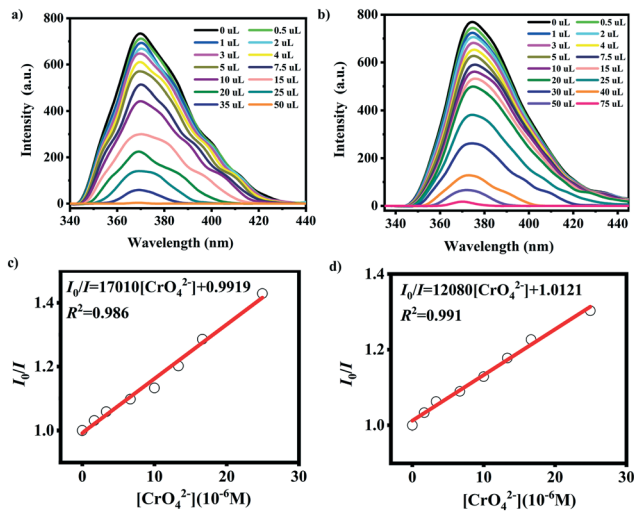


Fig. 13 Variation of luminescence intensities of **1** (a) and **3** (b) titrated with Na_2CrO_4 and the Stern–Volmer plots of CrO_4^{2-} in **1** (c) and **3** (d).

of antibiotics in water were also examined. In this work, five classes of the most common antibiotics were selected as models to investigate the antibiotics detection ability of **1** and **3**, including nitroimidazole antibiotics (metronidazole, MDZ; dimetridazole, DTZ), nitrofurantoin antibiotics (nitrofurantoin, NFT; nitrofurazone, NZF), chloramphenicols (chloramphenicol, CAP), sulfonamides (sulfadiazine, SDZ), and β -lactams (penicillin, PCL) (Scheme S3†). As shown in Fig. 14 and S22,† the nitrofurantoin antibiotics (NFT and NZF) exhibit drastic quenching effects on the luminescence of **1** and **3**, while the other antibiotics display relatively small influences on the luminescence intensity of **1** and **3**. The quenching orders of **1** and **3** to those antibiotics are $\text{NFT} > \text{NZF} > \text{CAP} > \text{MDZ} > \text{DTZ} > \text{SDZ} > \text{PCL}$. Subsequently, fluorescence titration experiments were performed to investigate the detection capability of **1** and **3** toward NFT and NZF in depth. As seen in Fig. 15 and 16, the fluorescence intensities of **1** and **3** are decreased progressively with the addition of NFT and NZF. And the SV plots fit linearly, with the K_{SV} values being $7.07 \times 10^{-4} \text{ M}^{-1}$ ($R^2 = 0.994$) for NZF, and $8.64 \times 10^{-4} \text{ M}^{-1}$ ($R^2 = 0.989$) for NFT for **1**; $2.00 \times 10^{-4} \text{ M}^{-1}$ ($R^2 = 0.983$) for NZF, and $3.87 \times 10^{-4} \text{ M}^{-1}$ ($R^2 = 0.992$) for NFT for **3**. At the same time, the LODs for NZF/NFT are $7.45 \times 10^{-6} \text{ M}/5.71 \times 10^{-6} \text{ M}$ for **1** and $2.44 \times 10^{-5} \text{ M}/1.19 \times 10^{-5} \text{ M}$ for **3**, respectively (Tables S6 and S7†). Such high K_{SV} values and

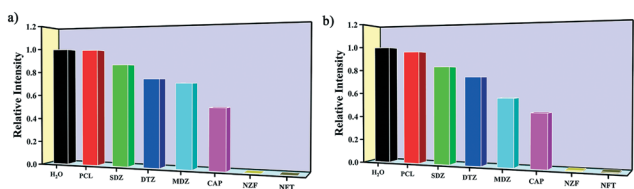


Fig. 14 Relative fluorescence intensity of **1** (a) and **3** (b) toward different antibiotics in H₂O solution.

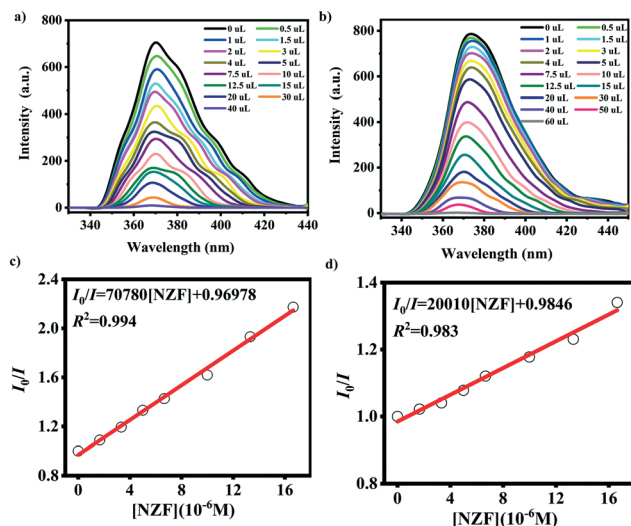


Fig. 15 Variation of luminescence intensities of 1 (a) and 3 (b) titrated with NZF and the Stern–Volmer plots of NZF in 1 (c) and 3 (d).

low detection limits are comparable to or lower than those previously reported (Table S9[†]).^{63–68}

Mechanism of luminescence sensing

To investigate the mechanism of the fluorescence quenching effect of 1 and 3 toward Fe^{3+} cation, $\text{Cr}_2\text{O}_7^{2-}/\text{CrO}_4^{2-}$ anions, and NZF/NFT antibiotics, few experiments were carried out. First, the PXRD patterns of the solid samples treated with Fe^{3+} cation, $\text{Cr}_2\text{O}_7^{2-}/\text{CrO}_4^{2-}$ anions, and NZF/NFT antibiotics solution are almost identical to the initial samples, confirming that the luminescence quenching was not caused by the collapse of the frameworks (Fig. S15[†]). Second, the UV-vis absorptions of Fe^{3+} , CrO_4^{2-} , and $\text{Cr}_2\text{O}_7^{2-}$ ions overlapped the emission peaks of the two Zn(II) CPs 1 and 3 than other anions (Fig. S23 and S24[†]), demonstrating

fluorescence quenching effects caused by Fe^{3+} cation and $\text{Cr}(\text{VI})$ anions, which can be ascribed to the resonance energy transfer (RET).^{69,70} As for the antibiotics, the excited electrons of CPs may transfer to the lowest unoccupied molecular orbital (LUMO) of antibiotics under excitation, leading to luminescence quenching. The calculated LUMO followed the order of NFT < NZF < CAP < MDZ < DTZ < SDZ < PCL (Fig. S25[†]). The lower LUMO value of antibiotics implies the easier electron transfer between CPs and analytes. The observed quenching efficiencies are almost consistent with the LUMO order; thus, the photo-induced electron transfer (PET) from two Zn(II) CPs to nitrofurantoin antibiotics (NFT and NZF) might have occurred and finally lead to luminescence quenching. Besides, the UV-vis absorption spectra of the two nitrofurantoin antibiotics (NFT and NZF) have the greatest overlap with the emission spectra of two Zn(II) CPs (Fig. S26[†]), which means that the resonance energy transfers (RETs) from Zn(II) CPs to nitrofurantoin antibiotics also contribute to the quenching effects. In other words, the electron transfer and energy transfer have combined to enable the high NFT and NZF fluorescence quenching effects than others.^{71–73}

Photocatalytic properties

To investigate the rapid removal or degradation of pollutants in aqueous phase, the conductivity of the designed 1–4 materials was measured using diffuse reflection to obtain the related band gap energy (E_g). As we all know, the E_g of the photocatalyst plays an important part in the photocatalytic process.^{74,75} Calculated by the Kubelka–Munk method, the E_g values are 2.84 eV for 1, 2.32 eV for 2, 2.75 eV for 3, and 2.27 eV for 4, manifesting the semiconducting features of these above mentioned crystalline materials (Fig. S27[†]), providing a theoretical basis for the titled four CPs as photocatalysts in the degradation of organic dyes. Methylene blue (MB) was selected as the model to evaluate the photocatalytic activities

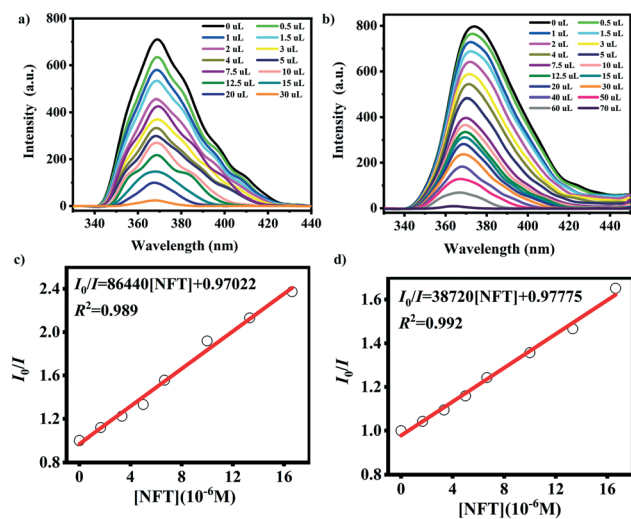


Fig. 16 Variation of luminescence intensities of 1 (a) and 3 (b) titrated with NFT and the Stern–Volmer plots of NFT in 1 (c) and 3 (d).

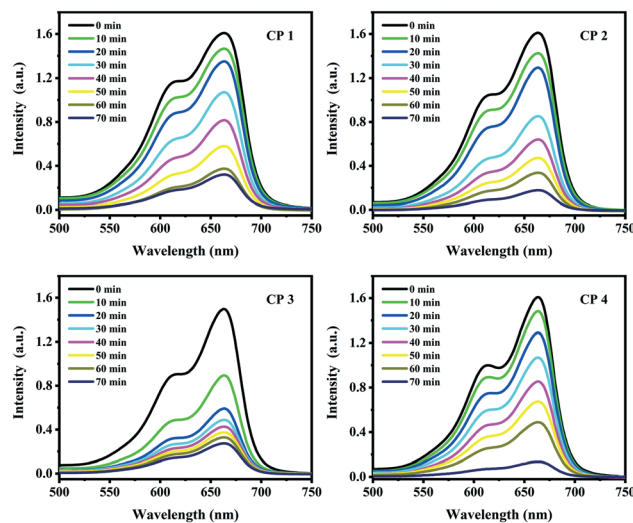


Fig. 17 UV-vis spectra of the photocatalytic degradation of MB with four CPs as photocatalysts.

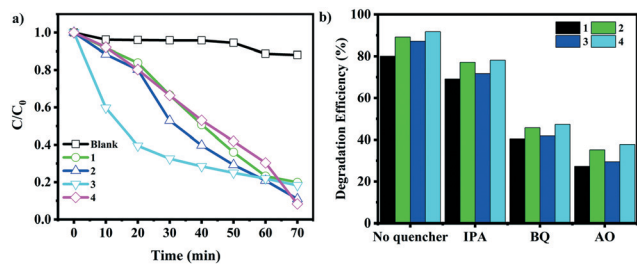


Fig. 18 (a) Photocatalytic decomposition of MB in aqueous solution under UV light irradiation using 1–4 and the control experiment without any catalyst; (b) trapping experiment of active species during the photocatalytic reaction of 1–4.

of 1–4 under UV irradiation. As illustrated in Fig. 17, the characteristic absorption peaks of MB decrease significantly as time goes on, with four CPs added as photocatalysts. Besides, the relationship between the concentration of MB and the reaction time in the presence or absence of 1–4 is shown in Fig. 18a. After 70 min MB dye cracking under UV irradiation, the degradation efficiencies are 80.1% for 1, 89.1% for 2, 81.7% for 3, 91.7% for 4, and 11.9% with H_2O_2 , respectively (Fig. 18). The photocatalytic activities of the four CPs follow the sequence of $4 > 2 > 3 > 1$, in line with the E_g values. After photocatalysis, the testing PXRD patterns of the four CPs are basically identical to the original ones, indicating the structures of 1–4 are stable during the photocatalytic process (Fig. S15[†]).

To explore the photocatalytic mechanism of the titled CPs in this work, benzoquinone (BQ), isopropyl alcohol (IPA), and ammonium oxalate (AO) were chosen as the scavengers for the superoxide ion ($\cdot O_2^-$), hydroxyl radicals ($\cdot OH$), and holes (h^+) to conduct the radical trapping experiments. The results indicated that the degradation efficiencies to MB are all reduced by some degree when the scavengers were added (Fig. 18b), with the efficiency changes of 80.1% to 69.1%, 40.5% and 27.3% for 1, 89.1% to 77.1%, 45.7% and 35.2% for 2, 81.7% to 71.1%, 41.8% and 29.5% for 3, and 91.7% to 78.1%, 47.3% and 37.8% for 4 in the presence of IPA, BQ and AO, respectively. Those results show that $\cdot OH$, $\cdot O_2^-$ as well as h^+ are the active species during the photocatalytic reaction. The possible mechanism of photodegradation of MB with the four CPs as photocatalysts was conjectured as follows.^{76,77} Upon UV irradiation, the electron (e^-) migration occurs from the HOMO to the LUMO of CPs. At the same time, an equal number of holes (h^+) are generated in the HOMO. To resume its stable state, h^+ reacts with H_2O_2 or H_2O molecules to manufacture $\cdot OH$ active constituent. Meanwhile, the e^- reacts with O_2 on the surfaces of CPs to generate superoxide radicals ($\cdot O_2^-$), which further translated into $\cdot OH$ radicals. Eventually, the formed $\cdot OH$ radicals could directly oxidize MB into CO_2 , H_2O , and other products.

Conclusion

In summary, four Zn(II)/Co(II) CPs were obtained based on the novel bifunctional ligand of 5-(6-carboxypyridin-2-yl)

benzene-1,3-dicarboxylic acid (H_3L) and two bis(imidazole) linkers. The final structures are 2D 4-c $\{4^4 \cdot 6^2\}$ **sql** wave sheet (1), **sql** sheet based 2D + 2D \rightarrow 2D interpenetrating sheets (2), 3D 2-nodal (4,4)-c $\{4^2 \cdot 8^3 \cdot 10\}$ **tcj** net (3), and novel 2D (3,4,4)-c $\{6^2 \cdot 7 \cdot 8^2 \cdot 10\}\{6^2 \cdot 7^3 \cdot 8\}_2\{6^3\}_2$ trilayer structure (4). The fluorescence measurements show that two Zn(II) CPs have high sensitivity in detecting Fe^{3+} cation, $Cr_2O_7^{2-}/CrO_4^{2-}$ anions, and NFT/NZF antibiotics in the aqueous solution. Further photocatalytic investigations illustrate that the four CPs hold outstanding potential as photocatalysts in the degradation of methylene blue (MB). In brief, the four CPs show potential applications in the detection and removal of pollutants in water.

Conflicts of interest

The authors declare no competing financial interest.

Acknowledgements

This work was supported by the National Natural Science Foundation of China (No. 21801230 and 21801218), Natural Science Foundation of Shanxi Province (No. 201801D0221084), Scientific and Technological Innovation Programs of Higher Education Institutions in Shanxi (No. 2019L0510), Young Academic Leader Supported Program of North University of China (No. QX201904), and the Opening Foundation of Key Laboratory of Laser & Infrared System (Shandong University), Ministry of Education (No. 2020-LISKFJJ-002).

References

- C.-C. Wang, X.-D. Du, J. Li, X.-X. Guo, P. Wang and J. Zhang, *Appl. Catal., B*, 2016, **193**, 198.
- V. K. Sharma and M. Feng, *J. Hazard. Mater.*, 2019, **372**, 3.
- Z. Hu, B. J. Deibert and J. Li, *Chem. Soc. Rev.*, 2014, **43**, 5815.
- H. Zhu, D. Liu, D. Zou and J. Zhang, *J. Mater. Chem. A*, 2018, **6**, 6130.
- Q. Wang, Q. Gao, A. M. Al-Enizi, A. Nafady and S. Ma, *Inorg. Chem. Front.*, 2020, **7**, 300.
- T. Zhang and W. Lin, *Chem. Soc. Rev.*, 2014, **43**, 5982.
- J. A. Zárate, E. Domínguez-Ojeda, E. Sánchez-González, E. Martínez-Ahumada, V. B. López-Cervantes, D. R. Williams, V. Martis, I. A. Ibarra and J. Alejandre, *Dalton Trans.*, 2020, **49**, 9203.
- Y. Pi, X. Li, Q. Xia, J. Wu, Y. Li, J. Xiao and Z. Li, *Chem. Eng. J.*, 2018, **337**, 351.
- X. Chen, R. Tong, Z. Shi, B. Yang, H. Liu, S. Ding, X. Wang, Q. Lei, J. Wu and W. Fang, *ACS Appl. Mater. Interfaces*, 2018, **10**, 32328.
- J. Lee, *CrystEngComm*, 2020, **22**, 8081.
- X.-Q. Wei, D. Shao, C.-L. Xue, X.-Y. Qu, J. Chai, J.-Q. Li, Y.-E. Du and Y.-Q. Chen, *CrystEngComm*, 2020, **22**, 5275.
- Y. Fang, J. A. Powell, E. Li, Q. Wang, Z. Perry, A. Kirchon, X. Yang, Z. Xiao, C. Zhu, L. Zhang, F. Huang and H.-C. Zhou, *Chem. Soc. Rev.*, 2019, **48**, 4707.

- 13 H. D. Park, M. Dinca and Y. Roman-Leshkov, *J. Am. Chem. Soc.*, 2018, **140**, 10669.
- 14 W. P. Lustig, S. Mukherjee, N. D. Rudd, A. V. Desai, J. Li and S. K. Ghosh, *Chem. Soc. Rev.*, 2017, **46**, 3242.
- 15 B. Yan, *Acc. Chem. Res.*, 2017, **50**, 2789.
- 16 J. Dong, D. Zhao, Y. Lu and W.-Y. Sun, *J. Mater. Chem. A*, 2019, **7**, 22744.
- 17 X. Chen, L. Shang, H. Cui, H. Yang, L. Liu, Y. Ren and J. Wang, *CrystEngComm*, 2020, **22**, 5900.
- 18 Z. Li, Z. Zhan and M. Hu, *CrystEngComm*, 2020, **22**, 6727.
- 19 S. Wu, M. Zhu, Y. Zhang, M. Kosinova, V. P. Fedin and E. Gao, *Chem. – Eur. J.*, 2020, **26**, 3137.
- 20 S. Xu, J.-J. Shi, B. Ding, Z.-Y. Liu, X.-G. Wang, X.-J. Zhao and E.-C. Yang, *Dalton Trans.*, 2019, **48**, 1823.
- 21 K. Zhu, R. Fan, X. Zheng, P. Wang, W. Chen, T. Sun, S. Gai, X. Zhou and Y. Yang, *J. Mater. Chem. C*, 2019, **7**, 15057.
- 22 X.-D. Zhang, J.-A. Hua, J.-H. Guo, Y. Zhao and W.-Y. Sun, *J. Mater. Chem. C*, 2018, **6**, 12623.
- 23 Z. Zong, C. Fan, X. Zhang, X. Meng, F. Jin and Y. Fan, *CrystEngComm*, 2019, **21**, 673.
- 24 J.-H. Li, X.-L. Wang, G. Song, H.-Y. Lin, X. Wang and G.-C. Liu, *Dalton Trans.*, 2020, **49**, 1265.
- 25 A.-L. Li, Y.-H. Qu, L. Fu, C. Han and G.-H. Cui, *CrystEngComm*, 2020, **22**, 2656.
- 26 J.-W. Cui, S.-X. Hou, Y.-H. Li and G.-H. Cui, *Dalton Trans.*, 2017, **46**, 16911.
- 27 Y. Liu, Y. Zhao, X.-H. Liu, Y.-S. Kang, P. Wang and W.-Y. Sun, *Dalton Trans.*, 2018, **47**, 15399.
- 28 Z.-Q. Liu, K. Chen, Y. Zhao, Y.-S. Kang, X.-H. Liu, Q.-Y. Lu, M. Azam, S. I. Al-Resayes and W.-Y. Sun, *Cryst. Growth Des.*, 2018, **18**, 1136.
- 29 Z.-Q. Liu, Y. Zhao, P. Wang, Y.-S. Kang, M. Azam, S. I. Al-Resayes, X.-H. Liu, Q.-Y. Lu and W.-Y. Sun, *Dalton Trans.*, 2017, **46**, 9022.
- 30 J. Wang, L. Gao, J. Zhang, L. Zhao, X. Wang, X. Niu, L. Fan and T. Hu, *Cryst. Growth Des.*, 2019, **19**, 630.
- 31 L. Qin, Q. Hu, Q.-M. Zheng, Y. Dou, H. Yang and H.-G. Zheng, *CrystEngComm*, 2020, **22**, 2327.
- 32 T.-R. Zheng, L.-L. Qian, M. Li, Z.-X. Wang, K. Li, Y.-Q. Zhang, B.-L. Li and B. Wu, *Dalton Trans.*, 2018, **47**, 9103.
- 33 Y. Zhao, X. Xu, L. Qiu, X. Kang, L. Wen and B. Zhang, *ACS Appl. Mater. Interfaces*, 2017, **9**, 15164.
- 34 X.-L. Wang, Y. Xiong, X.-T. Sha, G.-C. Liu and H.-Y. Lin, *Cryst. Growth Des.*, 2017, **17**, 483.
- 35 G. C. Liu, Y. Li, J. Chi, N. Xu, X. L. Wang, H. Y. Lin and Y. Q. Chen, *Dyes Pigm.*, 2020, **174**, 108064.
- 36 Z. Zong, C. Bi, Z. Zhu, C. Fan, X. Meng, X. Zhang and Y. Fan, *New J. Chem.*, 2018, **42**, 8905.
- 37 J.-Z. Gu, Y. Cai, X.-X. Liang, J. Wu, Z.-F. Shi and A. M. Kirillov, *CrystEngComm*, 2018, **20**, 906.
- 38 G. M. Sheldrick, *Acta Crystallogr., Sect. C: Struct. Chem.*, 2015, **71**, 3.
- 39 A. L. Spek, *Acta Crystallogr., Sect. C: Struct. Chem.*, 2015, **71**, 9.
- 40 V. A. Blatov, A. P. Shevchenko and V. N. Serezhkin, *J. Appl. Crystallogr.*, 2000, **33**, 1193.
- 41 H. Zhang, W. Jiang, J. Yang, Y.-Y. Liu, S. Song and J.-F. Ma, *CrystEngComm*, 2014, **16**, 9939.
- 42 R. Wang, X. Liu, A. Huang, W. Wang, Z. Xiao, L. Zhang, F. Dai and D. Sun, *Inorg. Chem.*, 2016, **55**, 1782.
- 43 S. Y. Hao, S. X. Hou, K. V. Hecke and G. H. Cui, *Dalton Trans.*, 2017, **46**, 1951.
- 44 J. Zhang, Y.-S. Xue, J. Bai, M. Fang, Y.-Z. Li, H.-B. Du and X.-Z. You, *CrystEngComm*, 2011, **13**, 6010.
- 45 B. Ding, Y.-Y. Wang, Y. You, S.-X. Liu, X.-X. Wu, Z.-Z. Zhu, J.-Z. Huo and Y.-Y. Liu, *CrystEngComm*, 2015, **17**, 5396.
- 46 A. Dey, A. Garai, V. Gude and K. Biradha, *Cryst. Growth Des.*, 2018, **18**, 6070.
- 47 S.-F. Tang and X. Hou, *Cryst. Growth Des.*, 2019, **19**, 45.
- 48 K.-Y. Wu, L. Qin, C. Fan, S.-L. Cai, T.-T. Zhang, W.-H. Chen, X.-Y. Tang and J.-X. Chen, *Dalton Trans.*, 2019, **48**, 8911.
- 49 L.-L. Qian, Z.-X. Wang, J.-G. Ding, H.-X. Tian, K. Li, B.-L. Li and H.-Y. Li, *Dyes Pigm.*, 2020, **175**, 108159.
- 50 J. Wang, N.-N. Chen, C. Zhang, L.-Y. Jia and L. Fan, *CrystEngComm*, 2020, **22**, 811.
- 51 P. Wu, L. Xia, F. Fu, M. Wang, B. Wen, Z. Yang and J. Wang, *Inorg. Chem.*, 2020, **59**, 264.
- 52 Y.-J. Yang, Y.-H. Li, D. Liu and G.-H. Cui, *CrystEngComm*, 2020, **22**, 1166.
- 53 J. Liu, Y. Ye, X. Sun, B. Liu, G. Li, Z. Liang and Y. Liu, *J. Mater. Chem. A*, 2019, **7**, 1683.
- 54 X. Zhang, H. Chen, B. Li, G. Liu and X. Liu, *CrystEngComm*, 2019, **21**, 1231.
- 55 J.-Y. Zou, L. Li, S.-Y. You, H.-M. Cui, Y.-W. Liu, K.-H. Chen, Y.-H. Chen, J.-Z. Cui and S.-W. Zhang, *Dyes Pigm.*, 2018, **159**, 429.
- 56 T. Wiwasuku, J. Boonmak, K. Siri Wong, V. Ervithayasuporn and S. Youngme, *Sens. Actuators, B*, 2019, **284**, 403.
- 57 M. Singh, S. Senthilkumar, S. Rajput and S. Neogi, *Inorg. Chem.*, 2020, **59**, 3012.
- 58 R. Lv, H. Li, J. Su, X. Fu, B. Yang, W. Gu and X. Liu, *Inorg. Chem.*, 2017, **56**, 12348.
- 59 C. Xu, C. Bi, Z. Zhu, R. Luo, X. Zhang, D. Zhang, C. Fan, L. Cui and Y. Fan, *CrystEngComm*, 2019, **21**, 2333.
- 60 X. Zhou, Y.-X. Shi, C. Cao, C.-Y. Ni, Z.-G. Ren, D. J. Young and J.-P. Lang, *Cryst. Growth Des.*, 2019, **19**, 3518.
- 61 C.-X. Wang, Y.-P. Xia, Z.-Q. Yao, J. Xu, Z. Chang and X.-H. Bu, *Dalton Trans.*, 2019, **48**, 387.
- 62 G. Liu, Y. Li, J. Chi, N. Xu, X. Wang, H. Lin, B. Chen and J. Li, *Dalton Trans.*, 2020, **49**, 737.
- 63 Q.-Q. Zhu, Q.-S. Zhou, H.-W. Zhang, W.-W. Zhang, D.-Q. Lu, M.-T. Guo, Y. Yuan, F. Sun and H. He, *Inorg. Chem.*, 2020, **59**, 1323.
- 64 Q.-Q. Zhu, H. He, Y. Yan, J. Yuan, D.-Q. Lu, D.-Y. Zhang, F. Sun and G. Zhu, *Inorg. Chem.*, 2019, **58**, 7746.
- 65 Y. Liu, Y. Zhao, Z.-Q. Liu, X.-H. Liu, X.-D. Zhang and W.-Y. Sun, *CrystEngComm*, 2020, **22**, 304.
- 66 Y. Zhang, J. Yang, D. Zhao, Z. Liu, D. Li, L. Fan and T. Hu, *CrystEngComm*, 2019, **21**, 6130.
- 67 R. Goswami, S. C. Mandal, N. Seal, B. Pathak and S. Neogi, *J. Mater. Chem. A*, 2019, **7**, 19471.

- 68 F. Guo, C. Su, Y. Fan and W. Shi, *Dalton Trans.*, 2019, **48**, 12910.
- 69 G. Liu, Y. Li, J. Chi, N. Xu, X. Wang, H. Lin, B. Chen and J. Li, *Dalton Trans.*, 2020, **49**, 737.
- 70 M. Wang, Z. Liu, X. Zhou, H. Xiao, Y. You and W. Huang, *Inorg. Chem.*, 2020, **59**, 18027.
- 71 Q. Chu, B. Zhang, H. Zhou, B. Liu, L. Hou and Y.-Y. Wang, *Inorg. Chem.*, 2020, **59**, 2853.
- 72 S. Gai, J. Zhang, R. Fan, K. Xing, W. Chen, K. Zhu, X. Zheng, P. Wang, X. Fang and Y. Yang, *ACS Appl. Mater. Interfaces*, 2020, **12**, 8650.
- 73 T. Sun, R. Fan, R. Xiao, T. Xing, M. Qin, Y. Liu, S. Hao, W. Chen and Y. Yang, *J. Mater. Chem. A*, 2020, **8**, 5587.
- 74 J. Liu, Y.-H. Tang, F. Wang and J. Zhang, *CrystEngComm*, 2018, **20**, 1232.
- 75 N. Xu, R.-L. Wang, D.-P. Li, X. Meng, J.-L. Mu, Z.-Y. Zhou and Z.-M. Su, *Dalton Trans.*, 2018, **47**, 4191.
- 76 J. Wang, N.-N. Chen, J. Qian, X.-R. Chen, X.-Y. Zhang and L. Fan, *CrystEngComm*, 2020, **22**, 6195.
- 77 J.-J. Liu, M.-H. You, M.-H. Li, C.-C. Huang and M.-J. Lin, *CrystEngComm*, 2020, **22**, 420.